






Psychoacoustic evaluation of different fan designs for an urban air mobility vehicle with distributed propulsion system^{a)}

Stephen Schade,^{1,b)}  Roberto Merino-Martinez,²  Antoine Moreau,¹  Susanne Bartels,³ 
 and Robert Jaron¹ 

¹German Aerospace Center, Institute of Propulsion Technology, 10625 Berlin, Germany

²Delft University of Technology, Faculty of Aerospace Engineering, 2629 HS Delft, the Netherlands

³German Aerospace Center, Institute of Aerospace Medicine, Linder Höhe, 51147 Köln, Germany

ABSTRACT:

Distributed propulsion systems are developed to power a new generation of aircraft. However, it is not known yet which noise emissions these propulsion systems produce, which psychoacoustic characteristics such systems exhibit, and how the generated noise is perceived. This paper investigates how fans with fewer stator than rotor blades affect the noise perception of a distributed propulsion system intended for an urban air mobility vehicle, which is equipped with 26 low-speed ducted fans. Three fan designs with different tonal to broadband noise ratio and opposite dominant noise radiation directions are examined. An analytical process is applied to determine the noise emission, propagate the sound through the atmosphere, auralize the flyover signals, and calculate psychoacoustic metrics. A validation and comparison with A320 turbofan engines at takeoff is provided. The results indicate that the distributed propulsion system generates noise signatures with complex directional characteristics and high sharpness. By applying tonal noise reduction mechanisms at source, a significant effective perceived noise level reduction is achieved for the considered fan stages with fewer stator than rotor blades. In addition, tonality, loudness and roughness are reduced well above one noticeable difference compared to a baseline fan and similar or even lower values are achieved than with turbofans. © 2025 Author(s). All article content, except where otherwise noted, is licensed under a Creative Commons Attribution (CC BY) license (<https://creativecommons.org/licenses/by/4.0/>).

<https://doi.org/10.1121/10.0036228>

(Received 1 November 2024; revised 26 February 2025; accepted 6 March 2025; published online 26 March 2025)

[Editor: Matthew Boucher]

Pages: 2150–2167

I. INTRODUCTION

Distributed propulsion systems represent an advancement in the design of future aircraft, offering new degrees of freedom compared to conventional concepts, for instance, regarding the number and arrangement of the engines on the airplane. These degrees of freedom cause new acoustic and psychoacoustic characteristics that may affect the noise perception. Therefore, there is a demand to investigate the noise emissions generated by distributed propulsion systems along with their psychoacoustic characteristics.

Typically, the acoustic design of fans is based on the assessment of individual sound pressure levels of a single engine. Moreover, the propulsors are commonly optimized considering the sound power levels at the source location (Giacche *et al.*, 2013; Jaron, 2018). This approach is consistent with the noise certification process as for the certification of new aircraft, a single value, the effective perceived noise level (EPNL) (measured in EPNdB), is evaluated. The EPNL is measured at takeoff, approach and flyover and designs with lower cumulative EPNL compared to a

reference value are targeted (EASA, 2023; ICAO, 2017). The evaluation of one cumulative EPNL primarily considers that newly certified aircraft are quieter than the specified reference level, however, the design with the lowest EPNL value may not necessarily be the one with the least annoying aural perception (Merino-Martinez *et al.*, 2024c; Rizzi, 2016; Torija and Clark, 2021). Consequently, newer aircraft may not sound more pleasant, even if they have a lower EPNL than conventional aircraft. Therefore, there is a need to assess the noise perception at an early stage within the design phase of new aircraft. For this purpose, it is necessary to develop fast and flexible models that can be incorporated into the acoustic preliminary design phase.

Human sound perception has been shown to not only depend on purely physical quantities (e.g., sound pressure or sound power level) but to a significant extent also on psychoacoustic characteristics, e.g., sharpness, spectral content and tonality for both conventional turbofan aircraft (Soeta and Kagawa, 2020; Torija *et al.*, 2019) and multicopter drone platforms (Gwak *et al.*, 2020; Merino-Martinez *et al.*, 2024c; Torija and Clark, 2021).

However, due to the specific characteristics of distributed fan concepts compared to conventional turbofan and multicopter drone concepts, the current knowledge about the

^{a)}This paper is part of a special issue on Advanced Air Mobility Noise: Predictions, Measurements, and Perception.

^{b)}Email: stephen.schade@dlr.de

relation between noise perception and physical as well as psychoacoustic parameters is not easily transferable to distributed fans. In general, there is little knowledge yet on how psychoacoustic parameters of modern urban air mobility (UAM) vehicles influence human perception. Boucher *et al.* (2024a) focused on rotorcraft-based UAM designs and found associations between psychoacoustics and perception partly contradicting prior assumptions (e.g., higher sharpness contributed to a more positive perception). To the best of the authors' knowledge, associations among physical characteristics, psychoacoustics, and perception of UAM vehicles with distributed ducted fans have not been reported yet.

The assessment of noise perception becomes particularly relevant for distributed propulsion systems with a large number of propulsors, as acoustic interaction, modulation, and interference effects influence the noise footprint (Bernardini *et al.*, 2020; Guérin and Tormen, 2023; Monteiro *et al.*, 2024; Pascioni and Rizzi, 2018; Schade *et al.*, 2024b). Sound perception is therefore a key factor for public acceptance of new aircraft concepts with distributed propulsion, which, for instance, are developed for UAM (Rizzi *et al.*, 2020). This is confirmed in a telephone survey which addressed the acceptance of airtaxis in Germany, where it was found that noise concerns negatively correlate with acceptance (Eißfeldt and Stolz, 2024).

For these reasons, acoustic effects need to be assessed in order to ensure that new propulsion systems are not only quieter than previous concepts but also sound more pleasant. In addition, there is a need to not only investigate individual noise levels of individual engines but also to consider the propulsion system as a whole, for example, as a combination of distributed fans in order to examine the noise signature and psychoacoustic characteristics of the entire propulsion system.

This paper examines the impact of fan design on the noise perception of a distributed propulsion system for an UAM aircraft. For this purpose, an analytical auralization [the acoustical counterpart of visualization (Vorländer, 2008)] framework, developed in house at the Department of Engine Acoustics, is first extended for distributed propulsion systems and then applied to the vectored thrust system of the UAM vehicle. As part of this tool chain, the fan noise emission is determined using Reynolds-averaged Navier Stokes- (RANS-) informed analytical noise prediction. Afterwards, virtual flyover simulations are performed to propagate the sound to specified microphone positions on the ground. The flyovers are then auralized using binaural noise syntheses. As a final step, based on the time signals, acoustic as well as psychoacoustic metrics are evaluated. Before applying this tool chain to the distributed propulsion system, the calculation of the noise immission and the psychoacoustic metrics is validated with measurement data from an A320 takeoff recorded near Schiphol Amsterdam Airport. Recently, this process has already been used to study the impact of speed fluctuations on the psychoacoustic characteristics of a distributed propulsion system (Schade *et al.*, 2024b).

The considered UAM concept airplane is equipped with 26 ducted, low-speed fan stages, where three fan designs are examined: (1) A conventional fan (treated as baseline) with more stator vanes than rotor blades, (2) a low-broadband noise fan (henceforth denoted as *low-broadband*) with fewer stator vanes than rotor blades, and (3) a low-tonal noise fan (henceforth denoted as *low-tone*) also with fewer stator vanes than rotor blades. The fan designs are similar with regard to aerodynamic characteristics, for example, efficiency, pressure ratio, and thrust (Schade *et al.*, 2024a). However, the fans provide different characteristics with regard to acoustics, for example, the dominant noise radiation direction and the tonal-to-broadband noise ratio. Due to these characteristics, the fan designs are particularly suitable for investigating acoustic and psychoacoustic effects and evaluating the impact on noise perception.

The manuscript is structured as follows: Section II A describes the design of the UAM concept vehicle. Section II B illustrates the different fan designs, as well as the integration of these fans on the vehicle. The auralization framework is described in Sec. II C. The limitations are outlined in Sec. III. The results are evaluated in Sec. IV, where Sec. IV A shows the validation with the A320 turbofan and Sec. IV B provides the transfer to distributed propulsion. The conclusions are summarized in Sec. V and an outlook is provided in Sec. VI.

II. MATERIAL AND METHODS

A. UAM concept vehicle

An UAM vehicle with distributed and tiltable ducted fans is conceptually designed to enable aeroacoustic studies. The design and sizing of the vehicle architecture are performed using an in-house simulation framework for vehicle and fleet assessments. This framework is first introduced by Shiva Prakasha *et al.* (2022) and is extended by Rätei *et al.* (2023) to derive optimal vehicle designs for different architectures and use cases. The basic tool for the conceptual design and sizing of such UAM vehicles with vertical take-off and landing (VTOL) capabilities is documented by Rätei (2022).

The top level aircraft requirements, which serve as an input for the design of the tilt-duct vehicle, are derived based on existing aircraft demonstrators and prototypes within the UAM market. In order to estimate the

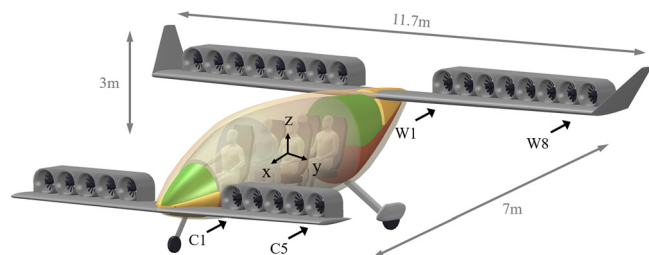


FIG. 1. Tilt-duct vehicle from project VIRLWINT for further high-fidelity disciplinary analysis and acoustic assessment.

TABLE I. Coordinates of the engine center position relative to the center of gravity of the UAM vehicle. Since the vehicle is symmetrical to the $y = 0$ m plane, only half of the engine positions are listed. C: canard wing; W: main wing.

Engine	x [m]	y [m]	z [m]
C1	2.65	1.2	-0.3
C2	2.65	1.67	-0.3
C3	2.65	2.14	-0.3
C4	2.65	2.61	-0.3
C5	2.65	3.08	-0.3
W1	-3.105	1.2	1.165
W2	-3.105	1.67	1.165
W3	-3.105	2.14	1.165
W4	-3.105	2.61	1.165
W5	-3.105	3.08	1.165
W6	-3.105	3.55	1.165
W7	-3.105	4.02	1.165
W8	-3.105	4.49	1.165

technology readiness level in the vehicle design process, an hypothetical entry into service in the timeframe 2030 – 2035 is assumed. The vehicle has VTOL capabilities and can carry a payload of up to 450 kg (four passengers and one pilot on board) over a range of 100 km at a cruise speed of 200 km/h while opposed to a headwind of 20 km/h. Additionally, a 20-min loitering reserve is included in the sizing process.

Figure 1 shows the final battery-electric tilt-duct vehicle design including its dimensions and a labeling of the individual fan stages, which are distributed over the canard and the main wings. The corresponding engine center positions are listed in Table I. Based on the thrust provided by the fan stages, their number is determined to ensure that the propulsion system can lift and accelerate the maximum takeoff weight of 2900 kg vertically during takeoff. As a result, the propulsion system consists of 26 low-speed fan stages, where 10 fans are installed on the canard wing and 16 on the main wing. Each fan has a diameter of 0.45 m.

The design process of the considered tilt-duct vehicle is outlined in more detail by Schade *et al.* (2025).

B. Distributed propulsion system

1. Low-speed ducted fan designs

For the distributed propulsion system of the tilt-duct vehicle, three different rotor-stator fan stages are designed and manufactured. All three fan designs are developed for experimental testing in the CRAFT (Co-/Contra Rotating Acoustic Fan Test) facility (Caldas *et al.*, 2022; Tapken *et al.*, 2021) from DLR. In the CRAFT facility, ducted fan stages with representative conditions (e.g., rotor tip Mach number and fan pressure ratio) for UAM engines can be investigated.

The first fan stage is the baseline fan, which has 18 rotor blades and 21 stator vanes [see Fig. 2(a)]. The blade count pairing of the baseline fan is designed such that the acoustic modes at the first blade passing frequency (BPF) are cut-on. In addition to the baseline fan, two low-count OGV (outer guide vane) fans are designed and manufactured (Schade *et al.*, 2024a). Contrary to conventional fan designs, low-count OGV fans have fewer stator vanes than rotor blades. Schade *et al.* (2024a) outlined the multidisciplinary optimization process to design both low-count OGV fan stages and illustrated that all three fans provide similar aerodynamic but considerably different acoustic characteristics. Thus, these fans are well-suited for acoustic and psychoacoustic comparisons. The first low-count OGV fan stage is equipped with 31 rotor blades and 10 stator vanes [see Fig. 2(b)]. This design is denoted as *low-broadband fan* hereafter. The second low-count OGV fan stage has 31 rotor blades and 21 stator vanes [see Fig. 2(c)]. This fan design is named *low-tone fan* subsequently.

2. Conceptual nozzle design

To theoretically integrate the CRAFT fans on the tilt-duct vehicle and operate them over a wide operating range, a variable nozzle geometry is required. As the tilt-duct vehicle is expected to perform the takeoff and ascending flight phase vertically, the thrust requirements and aerodynamic operating conditions of the fan stage strongly depart from each other at takeoff and during cruise. As a result, a variable-geometry system is necessary to cope with such a

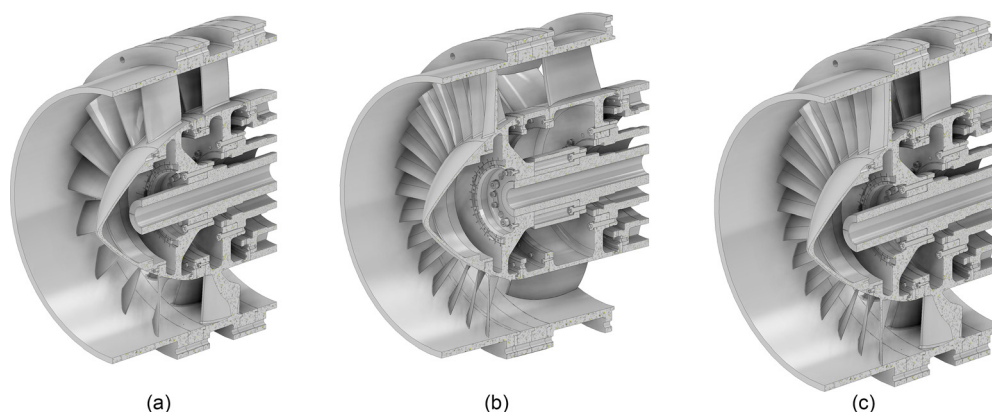


FIG. 2. Geometry of CRAFT baseline (a), low-broadband (b), and low-tone (c) fan stages.

TABLE II. Operating conditions and performance of the CRAFT stages when mounted on the tilt-duct vehicle.

	n [rpm]	n _{rel} [%]	\dot{m} [kg/s]	i_{rotor} [deg]	$M_{ax,in}$ [—]	$M_{rel,tip}$ [—]	PR [—]	η_{ise} [%]	SM [—]	altitude [m]	thrust [kN]
Cruise	3375	100	5.25	2	0.11	0.26	1.021	90.0	0.24	1520	2.1
Design	4500	133	6.98	2	0.14	0.31	1.038	90.5	0.24	—	—
Take-off fixed nozzle	8540	253	10.7	6.6	0.22	0.64	1.177	88.0	0.11	1520	30
Take-off VAN +30 %	7995	237	12.3	2	0.25	0.61	1.133	91.5	0.24	1520	30

wide operating range. A variable-area nozzle (VAN) is implemented at the conceptual design level according to the procedure described by Moreau *et al.* (2023b) and the results of the operating point calculations are shown in Table II, where n and n_{rel} define the rotational speed, \dot{m} is the mass flow rate, $M_{ax,in}$ is the inflow Mach number, $M_{rel,tip}$ is the rotor tip Mach number, and PR is the pressure ratio.

The predictions are performed considering the baseline fan stage only. However, the aerodynamics vary slightly between the baseline fan and the two low-count OGV designs, although the differences are small, as examined by Schade *et al.* (2024a), which is sufficiently accurate.

For the fan rotor blades to operate at an acceptable level of flow incidence angle (i_{rotor} , see Table II), the exhaust nozzle must be substantially opened during takeoff. The optimal opening ratio of 30% increased nozzle area was found according to the procedure by Moreau *et al.* (2023b), which provides the best fan isentropic efficiency (η_{ise} , see Table II) and a sufficient stability margin (SM) (see Table II) for the fan stage to operate safely away from its aerodynamic stall line. As shown in the aerodynamic performance map of the stage in Fig. 3, operating takeoff with an opened nozzle shifts the point onto the line of fan peak efficiency.

It should be noted at this point that the large excursion in mass flow and axial Mach number by a factor 2 or more from takeoff to cruise conditions (see Table II), requires a very careful design of the fan intake geometry in order to avoid flow separation at the intake lip, spillage drag, and additional inflow distortion noise. The design of the intake is not, however, considered within the scope of the present preliminary study.

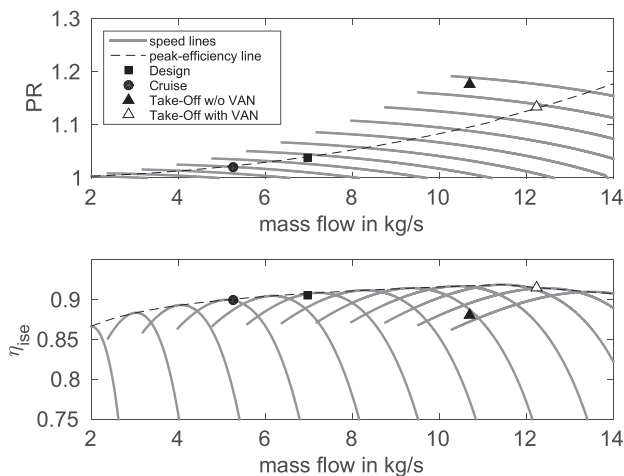


FIG. 3. Fan performance map of the CRAFT stages and position of the relevant operating points. Top: fan pressure ratio (PR), bottom: fan isentropic efficiency (η_{ise}).

C. Auralization framework

The auralization process consists of four steps which are visualized in Fig. 4. First, as described in Sec. IIC 1, the noise emission is predicted using the tool PropNoise (Propulsion Noise) (Moreau, 2017). Second, the noise immission is determined using virtual, acoustic flyover simulations performed with the tool VIOLIN (Virtual acoustic flyover simulation) (Dang, 2022). This is outlined in Sec. IIC 2. Third, as summarized in Sec. IIC 3, a binaural noise synthesis is applied to transfer the acoustic results into stereo audio files using the tool CORAL (Aircraft engine noise auralization) (Moreau *et al.*, 2023a). Finally, a sound quality assessment, as described in Sec. IIC 4, is applied which is conducted with the open-source toolbox SQAT (Greco *et al.*, 2024).

1. RANS-informed analytical noise prediction

For the present study, all acoustic sources are predicted using PropNoise (Moreau, 2017). PropNoise can either be applied as a stand-alone program or coupled with an external flow solver. The latter is used for the present study. For this purpose, PropNoise is coupled with the in-house flow solver TRACE (Yang *et al.*, 2006) in order to provide RANS-informed analytical noise predictions (Jaron, 2018). 3D steady-state RANS simulations are performed for each fan design (baseline, low-broadband and low-tone as visualized in Fig. 2) and both operating points (Cruise and Design from Table II). TRACE solves the compressible Navier-Stokes equations on a structured numerical grid using a multi-block approach. Regarding the numerical setup, an isolated fan with uniform inflow conditions is considered and the flow domain is a single rotor-stator passage with periodic boundary conditions. The Menter SST $k-\omega$

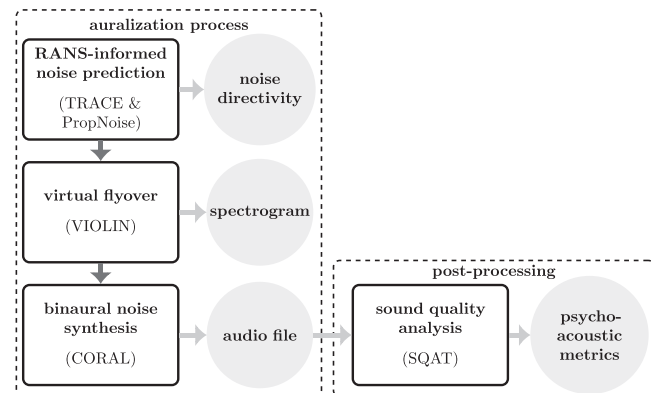


FIG. 4. Auralization process and post-processing.

turbulence model is applied since earlier studies showed that this model provides the best results with regard to the aerodynamic flow solution and analytical noise prediction than other turbulence models (Jaron, 2018). Regarding the numerical grid, an O-C-H topology is used around the blade/vane, where the first cell is placed in the laminar sub-layer. Further details regarding the numerical setup and grid as well as the aerodynamic flow solutions for the three fan designs can be obtained from Schade *et al.* (2024a).

The aerodynamic flow variables required to reconstruct the aerodynamic excitation that leads to noise generation are exported from the RANS simulations as radial distributions. These radial distributions are extracted along streamlines and are used as an input for PropNoise to determine the noise source generation and propagation analytically. PropNoise provides a frequency-formulation of all fan noise sources, whereby in this study only rotor–stator interaction noise is considered. The extracted radial distributions of aerodynamic flow variables provide the input for a radial strip approach to calculate the acoustic source terms. Based on the in-duct Green’s function \hat{g}_{mn}^ω , the modal sound pressure amplitude is determined from a radial integration of the acoustic source terms. For tonal noise, the complex modal sound pressure amplitudes are determined from

$$p_{mn}^\pm = i \cdot V \int_r^R \hat{g}_{mn}^\omega e^{-ik_x x_{LE} - im\theta_{LE}} \cdot \sigma_L \cdot dr_s \quad (1)$$

and for broadband noise, the deterministic quantity to consider is the expectation value of the squared modal sound pressure magnitude, which is obtained from

$$\langle |p_{mn}^\pm|^2 \rangle = V \int_r^R |\hat{g}_{mn}^\omega|^2 \cdot \langle |\sigma_L|^2 \rangle \cdot l \cdot dr_s, \quad (2)$$

where + is the downstream and – the upstream direction, V is the number of stator vanes, r is the hub and R the tip radius, k_x denotes the axial wave number, x_{LE} and θ_{LE} specify the leading edge position, σ_L denotes the source term for the lift-generated component, and l is the turbulence correlation length in radial direction (Moreau, 2017). Subsequently, the sound is propagated upstream and downstream through the duct segments of the fan stage and radiated from the entry and exit planes. The noise radiation results are then saved as directivity patterns on a hemisphere with a defined radius. A detailed description of the acoustic models used in PropNoise can be obtained from Moreau (2017) and the coupling between PropNoise and an external flow solver is described by Jaron (2018). Jaron (2018) also validated the RANS-informed noise prediction method for several fan stages using experimental and numerical results.

2. Virtual acoustic flyover simulation

The modal directivity patterns obtained from PropNoise serve as an input for the in-house tool VIOLIN. Using VIOLIN a virtual flyover simulation is performed and the

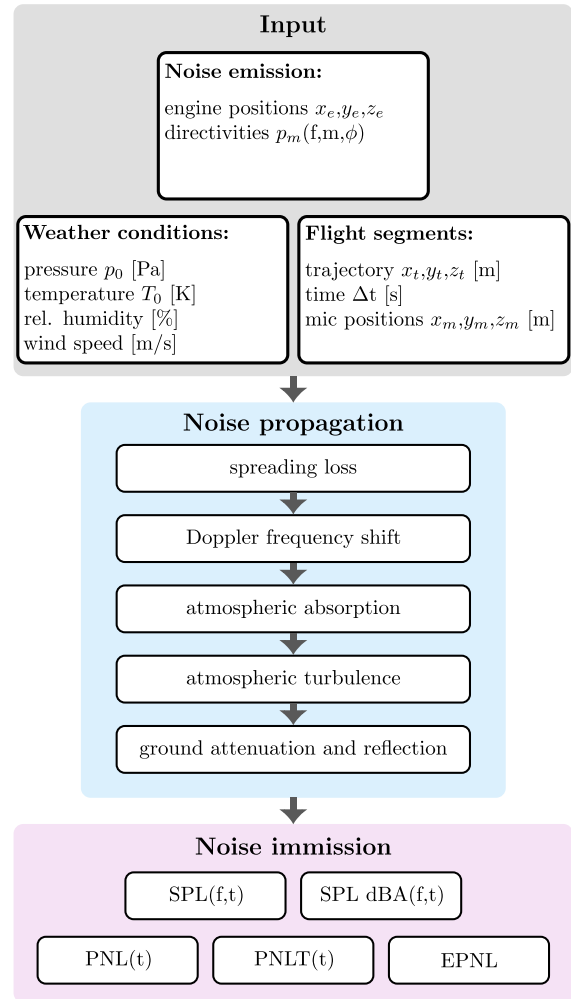


FIG. 5. Process chain for the virtual acoustic flyover simulation with VIOLIN.

noise is propagated through the atmosphere to one or several observer positions on the ground.

VIOLIN provides a frequency-domain formulation to determine the noise immission and accounts for the Doppler frequency shift, the atmospheric absorption (ISO 9613-1, 1993), the impact of atmospheric turbulence on amplitude as well as phase relations (Prescher *et al.*, 2024; Rietdijk *et al.*, 2017) and the attenuation as well as reflection of the sound waves on the ground (Arbeitsgruppe Novellierung der AzB, 2007; Hornikx, 2016). Figure 5 schematically illustrates this analytical process and Moreau *et al.* (2023a) provide an overview of the auralization process.

In order to account for distributed propulsion systems, VIOLIN is extended to consider multiple, distributed engines at arbitrary positions. The engine positions are defined relative to the center position of the airplane using xyz-coordinates specified in the airplane reference frame (see Table I).

An individual PropNoise calculation is assigned to each engine in each sub-segment of the flyover. Thus, individual RANS-informed analytical noise predictions (see Sec.

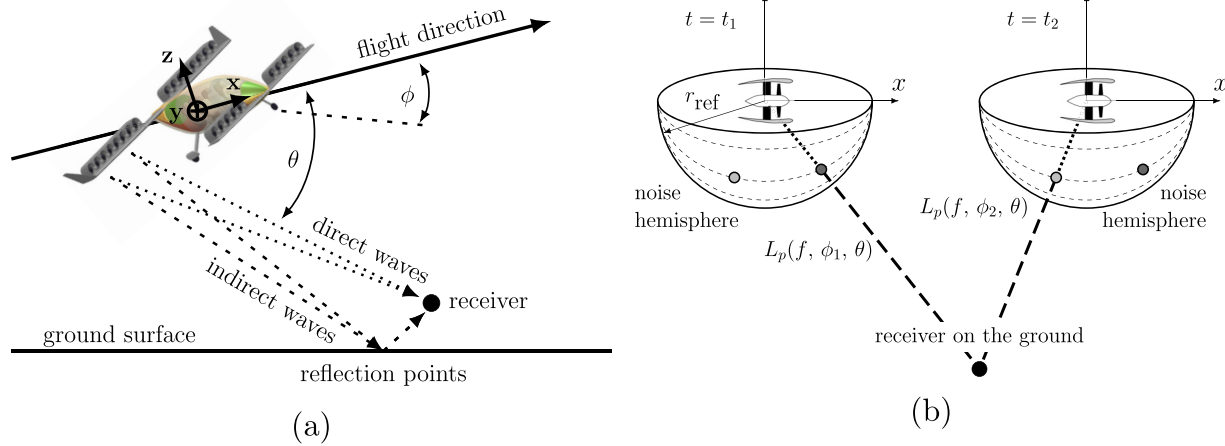


FIG. 6. Polar and lateral angles as a function of flyover time.

IIC1) are performed in advance for each engine. The present study uses steady engine operating conditions. This means that the operation point of each engine does not change during flyover. Consequently, 26 PropNoise calculations are performed (one for each engine) and assigned to the distributed propulsion system. For tonal noise sources, complex pressure amplitudes are assigned [see Eq. (1)] and for broadband sources, absolute squared amplitudes are considered [see Eq. (2)], whereby these are imported as narrow-band power spectral densities with logarithmic frequency distribution. As an initial step, the broadband values are converted to complex pressure amplitudes using $p_{mn}^{\pm} = \sqrt{\langle |p_{mn}^{\pm}|^2 \rangle} \cdot e^{-i\theta}$. This is done only for broadband sources, as for tonal sources, complex pressure amplitudes are directly obtained from PropNoise.

PropNoise determines the noise directivities radiated to a hemisphere of specified radius r_{ref} in the far field for each noise source. To provide the pressure amplitudes at arbitrary receiver distances and positions, a distance correction is implemented in VIOLIN (denoted as spreading loss in Fig. 5). Thereby it is assumed that the tonal/broadband amplitudes are inversely proportional to the propagation distance. Afterwards, the polar and lateral emission angles (ϕ and θ) are calculated for each engine at each time step [see Fig. 6(a)]. Using an interpolation method the respective tonal/broadband amplitudes are extracted from the noise hemispheres based on the calculated emission angles at each time step [see Fig. 6(b)]. With the extracted amplitudes the direct and indirect sound waves are propagated through the atmosphere to the receiver position on the ground considering the mentioned noise propagation effects (see blue box in Fig. 5). For the superposition of the direct and indirect sound waves, a phase relation is included for both tonal and broadband sources. Depending on the travel distance difference Δr between the direct and indirect sound waves, the complex amplitudes of the indirect waves are obtained from $p_{\text{indirect}} = p_{mn}^{\pm} e^{-i2\pi[f_{\text{Doppler}}/c]\Delta r}$, where f_{Doppler} are the Doppler-shifted frequencies and c is the speed of sound. At the

reflection point, the assumption is made that the ground is an acoustically hard surface. In addition to interferences resulting from the travel distance difference, no further interferences are calculated for broadband sources, as this source is assumed to be uncorrelated.

For tonal noise sources, the noise propagation may be strongly affected by interferences. Tonal sources are assumed fully correlated in VIOLIN and their linear superposition is carried out according to the method by Guérin and Tormen (2023). Thus, the complex tonal noise directivity $D_m(f, r_{\text{ref}}, \phi)$ obtained from PropNoise is modified as follows:

$$p_m(f, \phi, \theta) = D_m(f, r_{\text{ref}}, \phi) e^{im\theta}, \tag{3}$$

where θ is the lateral emission angle, r_{ref} is the specified reference radius for noise radiation in PropNoise, and m is the vector containing the azimuthal modes according to the Tyler and Sofrin relation (Tyler and Sofrin, 1962). With $m = hB - kV$ and $hB = f/n$, Eq. (3) can be reformulated as

$$p_m(f, \phi, \theta) = D_m(f, r_{\text{ref}}, \phi) e^{i(m-f/n)(\theta - \Delta\theta_{\text{stat}})} e^{i(f/n)(\theta - \Delta\theta_{\text{rot}})}, \tag{4}$$

where f is the blade passing frequency vector and n is the rotational speed. This formulation is implemented in VIOLIN as it allows considering the following effects: First, the rotation direction of individual propulsors can be changed by inverting the sign of the azimuthal mode vector m . Thus, counter-rotating configurations can also be considered. Second, the term $(\theta - \Delta\theta_{\text{stat}})$ and the term $(\theta - \Delta\theta_{\text{rot}})$ can be used to modify, respectively, the clocking position of the stator and rotor compared to the reference position from PropNoise. Thereby $\Delta\theta_{\text{stat}}$ describes the angle difference for the stator and $\Delta\theta_{\text{rot}}$ the angle difference for the rotor. For the present study, $\Delta\theta_{\text{rot}}$ is randomized once between the 26 fan stages, and one identical random distribution is applied to all flyover cases. Regarding the stator clocking positions, $\Delta\theta_{\text{stat}} = 0$ is applied to all fan stages. This is reasonable, as the position of the stator vanes can be controlled by design,

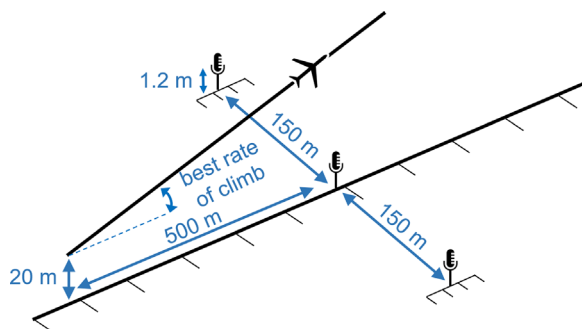


FIG. 7. Take-off reference procedure according to EASA specifications for VTOL aircraft (EASA, 2023).

unlike those of the rotor blades that may vary from flight to flight. The trajectory segment for the virtual flyover simulation is selected according to the EASA specifications for VTOL aircraft powered by tilting rotors (EASA, 2023). The takeoff reference procedure, as visualized in Fig. 7, is selected to compare the three fan designs. The flight Mach number is $M_{\text{take-off}} = 0.18$ and the rate of climb is $\alpha_{\text{climb}} = 6^\circ$. Moreover, the flyover is performed for a simulation time of $t = 21$ s and the time discretization is $\Delta t = 0.015$ s. In accordance with the EASA specifications (EASA, 2023), the atmospheric pressure is 101, 325 Pa, the ambient air temperature is 25°C and the relative humidity is 70%.

Design conditions are assigned to each engine as listed in Table II. According to the findings from Schade *et al.* (2024b), a fixed random distribution of rotational speed deviations within the range $\pm 1\%$ is applied to the distributed engines. Therefore, prior to calculating the noise emission with PropNoise, a speed variation within the range of $\pm 1\%$ relative to the nominal speed is randomly determined for each engine. These speed variations are interpreted as a constant deviation from the nominal rotational speed. Thus, one PropNoise calculation is performed for each engine using the determined rotational speed. Afterwards, for the flyover simulation, each PropNoise calculation is assigned to the corresponding engine. Thereby it is assumed that the speed deviations are static and thus do not change during flyover. Since these deviations are very small, tonal noise is still assumed to be correlated. The impact of different sets of speed deviations, which are applied to the 26 ducted fans, on the noise immission results and the sound quality analysis is assessed in Schade *et al.* (2024b).

As an output from VIOLIN, for tonal noise sources, the spectrograms are provided as complex pressure amplitudes, whereas for broadband noise sources the output spectrograms do not include phase information.

3. Binaural noise synthesis

The spectrograms obtained from VIOLIN are the input for the in-house auralization tool CORAL (Moreau *et al.*, 2023a). Using CORAL, a binaural noise synthesis is applied to transform the spectrograms into time signals for the right and left ear. Since tonal noise sources are assumed as correlated whereas broadband sources are considered

uncorrelated, CORAL processed these noise sources separately. Tonal sources are synthesized using an additive process and broadband sources using a subtractive process involving the filtering of a white noise signal, as described by Moreau *et al.* (2023a). Head related impulse responses (HRIRs) are used to transfer the monaural time series into stereo signals. The HRIRs represent transfer functions that contain all binaural and spectral characteristics resulting from the interaction of a head with an incoming sound wave. As the primary goal in CORAL is to achieve plausible and realistic binaural auralizations and not to reproduce the exact response of a specific head, no individual HRIRs are measured or simulated, but artificial head HRIRs are used. For this, a far-field data set, measured by Bernschütz (2013), is considered. Based on the relative position between the UAM vehicle and the observer, the two matching HRIRs of the left and right ear are selected from the data set. As a result, a binaural audio signal is generated that represents the sound of a UAM vehicle moving in space. The audio file is stored in Waveform Audio file format (.wav file).

4. Sound quality analysis

Sound quality metrics (SQMs) describe the subjective perception of sound by human hearing, unlike the L_p metric, which quantifies the purely physical magnitude of sound based on pressure fluctuations. Previous studies (Merino-Martinez *et al.*, 2021; Merino-Martinez *et al.*, 2022) showed that these metrics better capture the auditory behavior of the human ear compared to conventional sound metrics typically employed in noise evaluations. The five most commonly used SQMs (Greco *et al.*, 2023b; Merino-Martinez *et al.*, 2024a) are as follows.

- Loudness (N): Subjective perception of sound magnitude corresponding to the overall sound intensity (ISO 532-1, 2017).
- Tonality (K): Measurement of the perceived strength of unmasked tonal energy within a complex sound (Aures, 1985).
- Sharpness (S): Representation of the high-frequency sound content. In general, frequencies higher than 3 kHz are perceived as sharper (von Bismark, 1974).
- Roughness (R): Hearing sensation caused by sounds with modulation frequencies between 15 and 300 Hz (Daniel and Webber, 1997).
- Fluctuation strength (FS): Assessment of slow fluctuations in loudness with modulation frequencies up to 20 Hz, with maximum sensitivity for modulation frequencies around 4 Hz (Osses Vecchi *et al.*, 2017).

These five SQMs were calculated for each audio recording and their 5% percentile values were considered (hence the “5” subindex henceforth), representing the value of each SQM exceeded 5% of the total recording time. These 5% percentile values were then combined into global psychoacoustic annoyance (PA) metric following the model outlined by Di *et al.* (2016). All SQMs, the PA metric, and

conventional sound metrics (e.g., equivalent A-weighted sound pressure level $L_{p,A,eq}$ and EPNL) were calculated using the open-source MATLAB toolbox SQAT (Sound Quality Analysis Toolbox) v1.1 (Greco *et al.*, 2024). The GitHub repository of the toolbox can be found in Greco *et al.* (2023a).

III. LIMITATIONS

- Analytically determined noise directivities are used as an input for the flyover simulation. In order to improve the results, measured directivities should also be considered as an input in future studies.
- Installation effects such as boundary layer ingestion or noise shielding are neglected although, according to the vehicle design, the fan stages are located on the wings.
- As take-off trajectories are used, it is assumed that the engines are the dominant noise sources. To determine the noise emission of the ducted fans of the UAM vehicle, broadband and tonal rotor–stator interaction noise as well as trailing edge noise are considered. Airframe, background, and other engine noise sources are neglected.
- Since only one sub-segment of the take-off flight phase is simulated, steady engine operating conditions are applied, although the vehicle is accelerating during take-off.
- Vehicle and wing angle of attack changes are not accounted for.
- Liners are not included.
- With regard to the three examined fan designs, only the noise emission levels of the baseline design are validated with measurement data yet (Schade *et al.*, 2024a). The validations of the noise levels of the low-broadband noise and low-tonal noise designs are not included in this study as the respective measurement campaign is not accomplished yet.
- The psychoacoustic annoyance model by Di *et al.* (2016) applied here is already an improved model of the original model developed by Fastl and Zwicker (2007) based on synthetic sounds but also data from listening tests with technical sounds, e.g., car noise, air conditioner or factory noise. However, it remains open to what extent this model is also valid for new sounds from UAM vehicles. For a more accurate evaluation on the perceptual differences between the three fan designs, psychoacoustic listening experiments are recommended.

IV. RESULTS AND DISCUSSION

A. Validation of the auralization framework

In order to provide a qualitative and quantitative validation of the analytical auralization framework (see Fig. 4), a virtual flyover of two turbofan engines is compared with an experimental acoustic measurement of an Airbus A320 take-off recorded near Schiphol Amsterdam Airport, in the Netherlands. The aircraft was equipped with two IAE V2527-A5 turbofan engines.

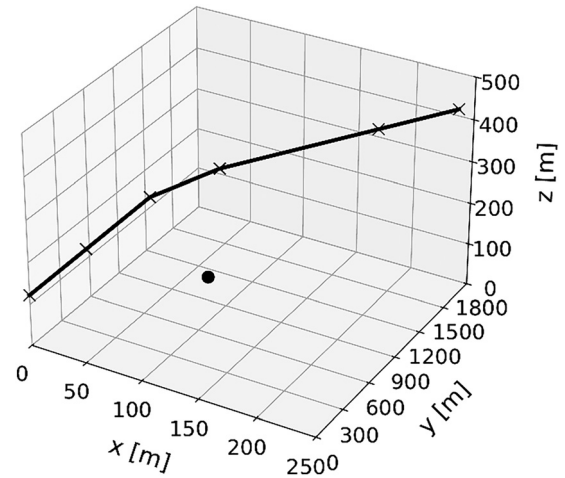


FIG. 8. Flight trajectory and microphone position (denoted as a black dot) for the Airbus A320 takeoff.

For the validation of the auralization framework, the following additional assumptions and limitations apply.

- The noise immission and the sound quality metrics are compared between analytical prediction and measurement for a single A320 take-off at a single microphone. Thereby it is neglected that differences can also occur with regard to the noise levels at source. These data are not part of the flyover measurement so that a comparison was not possible.
- Regarding the operating conditions, a retrofit is performed based on the experimental measurement data for an equivalent Airbus A320-like engine with similar design parameters. Thereby, the rotational speed is reconstructed from the number of blades and the frequency of the BPF in the measurement. Mass flow, blade angle, and nozzle area are selected so that the aerodynamic operating point of the engine is plausible (e.g., small incidence on fan blades).
- The following noise sources are considered: fan buzz-saw noise, jet noise and fan broadband noise. Fan tonal noise is neglected due to two main reasons: Firstly, the BPF tone is cut-off due to the larger amount of stator vanes than rotor blades. Secondly, for the measurement case, the second harmonic of the BPF is efficiently attenuated by a liner since it is not visible in the spectrogram [see Fig. 9(a)]. However, the BPF2 would be cut-on in the simulation and dominantly contribute to the noise radiation as it was out of scope for this work to include a realistic liner geometry. Consequently, to ensure comparability between measurement and prediction, the fan tones were neglected altogether.
- For the atmospheric conditions, an ambient air temperature of 290 K, a pressure of 102 710 Pa, a relative humidity of 45% and a wind speed of $u_x = u_y = 1.2$ m/s are applied. These data are in accordance with the respective measurement day.

The microphone employed is a PUI Audio POM-2735P-R analog condenser microphone with a sensitivity of -35 ± 2 dB (ref. 1 V/Pa) and a frequency range of 20 Hz to

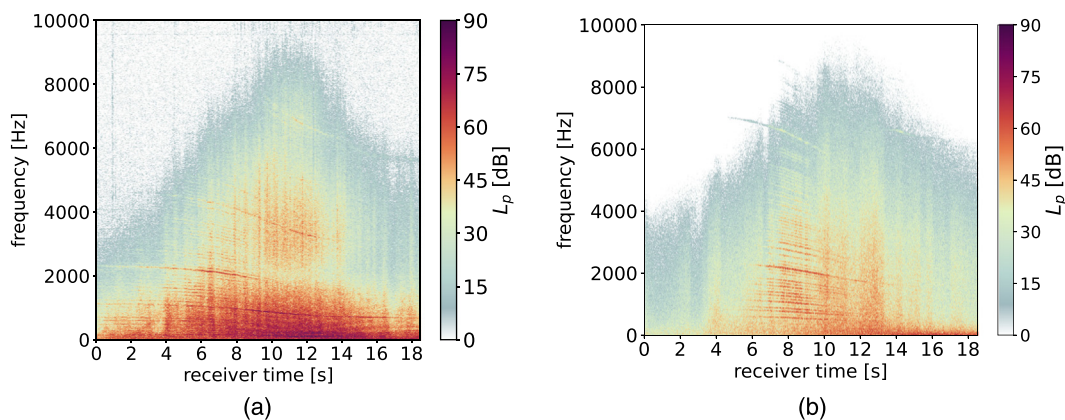


FIG. 9. Comparison between the measured (a) and simulated (b) spectrograms of the Airbus A320 takeoff. Color scheme specifically developed for the visualization of noise emission and immission according to Weninger (2015).

25 kHz. The sampling frequency employed is 50 kHz. The microphone was positioned at a small lateral offset to the flight path. To mitigate ground reflections, the microphone is placed directly on the ground and placed over a 15-mm layer of acoustic-absorbing foam. Figure 8 depicts the Airbus A320 takeoff flight path estimated from the Automatic Dependent Surveillance-Broadcast (ADS-B) data collected from OpenSky’s database (OpenSky, 2025). At the moment of the closest distance to the microphone (equivalent to overhead), the aircraft’s altitude was 121.92 m. More information about the experimental setup can be found in Merino-Martinez et al. (2024b).

Figure 9 presents the comparison between the measured and simulated spectrograms of the Airbus A320 takeoff. Overall, a good qualitative agreement is achieved and the overall shape of the spectrogram is reproduced from the virtual flyover simulation. The characteristic shape is mainly affected by atmospheric absorption and atmospheric turbulence, which are both well-predicted compared to the measurement case. The impact of atmospheric attenuation is evident in the lower noise levels at high frequencies and the impact of atmospheric turbulence is visible as vertical interference stripes.

The different noise sources can be identified in specific sections of the spectrogram. Buzz-saw noise is visible between 5 and 10 s and is observed as a low-frequency tone

and several of its harmonics. To predict buzz-saw noise a random variation of fan rotor stagger angles within the range $\pm 0.3^\circ$ is applied. Compared to the measurement data, the frequencies of the buzz-saw tones agree well, however, the noise levels are slightly overestimated. This is reflected in higher sound pressure amplitudes [see Fig. 10(a) at $7\text{ s} < t < 10\text{ s}$] and higher $L_p(t)$ as well as PNL(t) values [see Fig. 10(b) at $7\text{ s} < t < 10\text{ s}$].

For both measurement and prediction, jet noise is particularly visible in the spectrograms within the low-frequency range after the microphone is passed. Whereas in the measured spectrogram jet noise is the dominant source within the time range between 10 and 12 s, in the predicted spectrogram jet noise occurs over a larger time interval (see 10–18 s). This is again reflected in the time signals, where for the measurement case the highest amplitudes occur at 12 s, and for the prediction almost equal amplitudes are observed between 10 and 18 s [see Figs. 10(a) and 10(b)]. Regarding low-frequency noise, it should be noted that the measured data has background noise (typically dominant at very low frequencies) that is not included in the simulated case.

Figure 11 shows the comparison between measurement and prediction for the SQMs calculated using SQAT (see Sec. II C 4). The “just noticeable differences” (JND) are plotted as an error bar from the measurement case. The

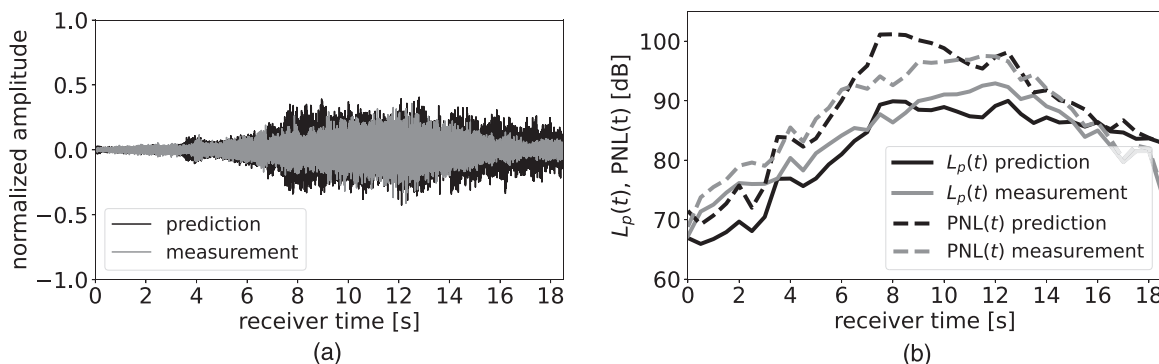


FIG. 10. Comparison between the measured and simulated time signals (a) and the sound pressure levels as well as perceived noise levels (b) of the Airbus A320 takeoff.

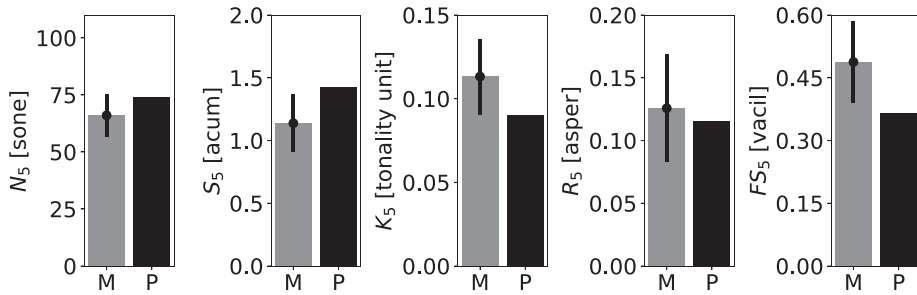


FIG. 11. Comparison of the SQMs between measurement and prediction of the Airbus A320 takeoff. M: measurement; P: prediction. For the measurement case, the error bars refer to the just noticeable differences (JND), where each error bar is plotted as \pm JND.

underlying hypothesis for the JNDs is that sounds differing by more than one JND are detected as different, so that Δ JND values can be obtained for each SQM as suggested by Osses *et al.* (2023). Considering that background noise and airframe noise are not included in the prediction, differences are within an acceptable range. The largest differences occur for the tonality metric. This was expected as fan tonal noise was neglected for the simulation, as aforementioned. However, this assumption is only valid for the BPF tone and its second harmonic since in the measured spectrogram the fourth harmonic of the fan BPF is visible at $t = 12$ s and $f = 7000$ Hz, while this fan tone was excluded from the simulation. In addition, for the measurement, the buzz-saw tones occur over a longer time interval compared to the prediction. Consequently, for these two reasons, the measured spectrogram consists of a slightly higher tonal energy than the prediction, and, hence, the higher tonality value is obtained. The binaural audio file of the synthesized flyover is available in Mm. 1.

Mm. 1. Binaural audio file of the synthesized flyover of the turbofan engines at takeoff. File of type “wav.”

B. Distributed propulsion system with ducted fans

1. Noise emission

The noise emission describes the noise that occurs at the noise source. In this section, noise emissions of the individual fans are examined first and, subsequently, the distributed propulsion system consisting of 26 ducted fans is analyzed. Figure 12 depicts the tonal and broadband frequency spectra of the three considered fan stages at design operating conditions. The broadband spectra are presented as one-third-octave bands.

Regarding the baseline fan, the frequency spectrum is dominated by the first BPF tone occurring at 1350 Hz and its second (2700 Hz) and third (4050 Hz) harmonics. All three fan tones provide significantly higher sound power levels than the broadband levels, therefore, the overall noise emission is dominated by tonal noise for this fan. For the low-broadband fan, the first BPF tone is raised to 2325 Hz since the number of rotor blades is increased from 18 to 31. The first BPF tone is still dominant although its sound power level is reduced by 11 dB compared to the first BPF of the baseline fan. In addition, the broadband noise levels are evenly reduced across the entire frequency range compared

to baseline and low-tone fans. The reduced broadband levels result from the lower number of stator vanes which is decreased from 21 to 10. The reason is that the broadband noise source is directly proportional to the number of stator vanes (Moreau, 2017; Nallasamy *et al.*, 2002). As a rule of thumb, the overall broadband noise levels decrease by approximately 3 dB if the number of stator vanes is halved (Jaron, 2018), which is valid for this fan design in good approximation.

For the low-tone fan, the first BPF tone is (inverse) cut-off (Schade *et al.*, 2024a; Schade *et al.*, 2022). The second BPF tone at 4650 Hz has similar noise levels compared to the broadband levels, and the third BPF tone is masked by broadband noise. As a result, for this fan, the overall noise emission is dominated by broadband noise, whereas for the baseline and the low-broadband fan the overall noise emission is dominated by tonal noise.

Figures 13 and 14 show the broadband and tonal noise directivities for the distributed propulsion system of the tilt-duct vehicle. The 26 fan stages are operated at design conditions. The noise levels are shown on a hemisphere with a radius of 100 m. The axial angle ϕ and the lateral angle θ are discretized using 180 points in each direction and $\phi = 180^\circ$ indicates the upstream direction and $\phi = 0^\circ$ is the downstream direction. It should be noted that the pictogram of the vehicle is enlarged for a better illustration.

The broadband noise source is modeled as constant in the lateral direction. Therefore, the broadband noise directivities are plotted in xz-plane and a stripe-shaped pattern is obtained (see Fig. 13). In addition, the overall shape of the broadband directivity is independent of the fan design. The directivity is characterized by two noise radiation maxima:

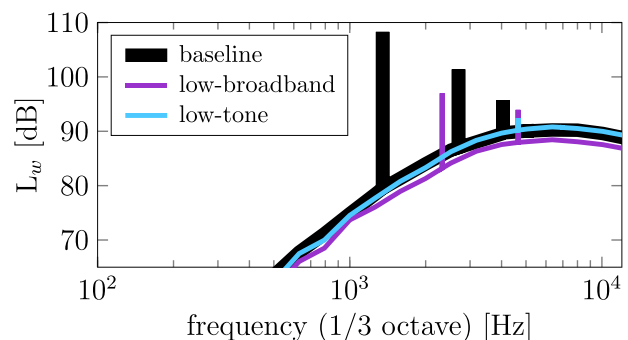


FIG. 12. Sound power spectra of the three considered fan stages at design conditions, $\theta = 90^\circ$ and a reference distance of 100 m.

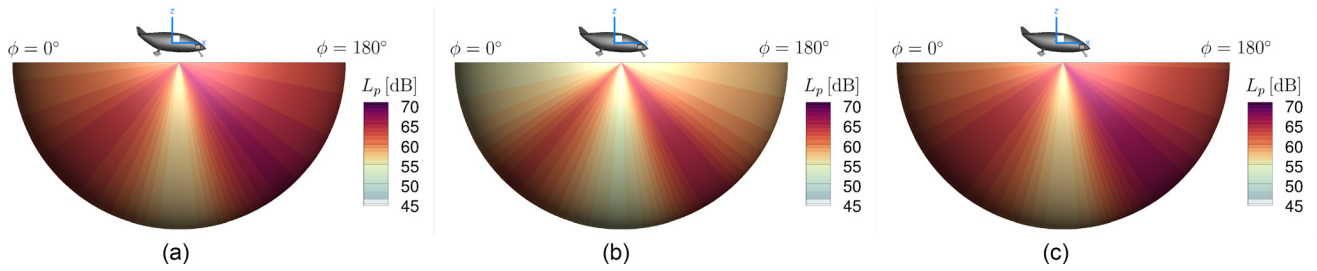


FIG. 13. Broadband noise directivities in the xz -plane at design conditions for the distributed propulsion system equipped with the baseline fan (a), low-broadband fan (b), and low-tone fan (c). Color scheme according to [Weninger \(2015\)](#).

A global maximum upstream at $\phi = 135^\circ$ and an additional maximum downstream at $\phi = 45^\circ$. The position of these maxima agree well with the expected result from the analytical modeling ([Heidmann, 1975](#)). For the low-broadband fan, the noise levels are evenly reduced over all radiation angles compared to the baseline and low-tone fan stages.

The tonal noise directivities are plotted in xy -plane and a strong dependence on the axial as well as the lateral angle is obtained (see Fig. 14). Overall, for tonal noise, directivities with complex interference patterns are obtained. The directivities are mainly characterized by “granulated” structures. In order to understand the formation of these structures, in a preliminary study, not shown here, the influence of the number of fan stages on the directivity was investigated. It was observed that the tonal noise directivity becomes more complex as the number of fans increases and that the granulated pattern is strongly impacted by the amount of fan stages. By increasing the number of fan

stages continuously from 2 to 26 it was observed that the tonal radiation pattern gradually “converges” to a complex interference pattern. Once a certain number of fan stages is reached (in our case more than 16), the interference pattern only slightly changed if additional fan stages are added to the distributed propulsion system. Thus, the system starts to behave like one distributed noise source rather than several individual and independent point sources. As a reference, for an individual baseline, low-broadband and low-tone fan, the tonal and broadband noise directivities can be obtained from [Schade et al. \(2025\)](#). Two additional effects also impact the interference pattern: First, due to the three-dimensional distribution of the fan stages, the Doppler shifted frequencies slightly deviate from each other leading to additional interference and modulation effects. Second, in order to provide a realistic, non-perfect tolerance between the operating conditions of the fan stages, one identical random distribution of speed deviations within the range of

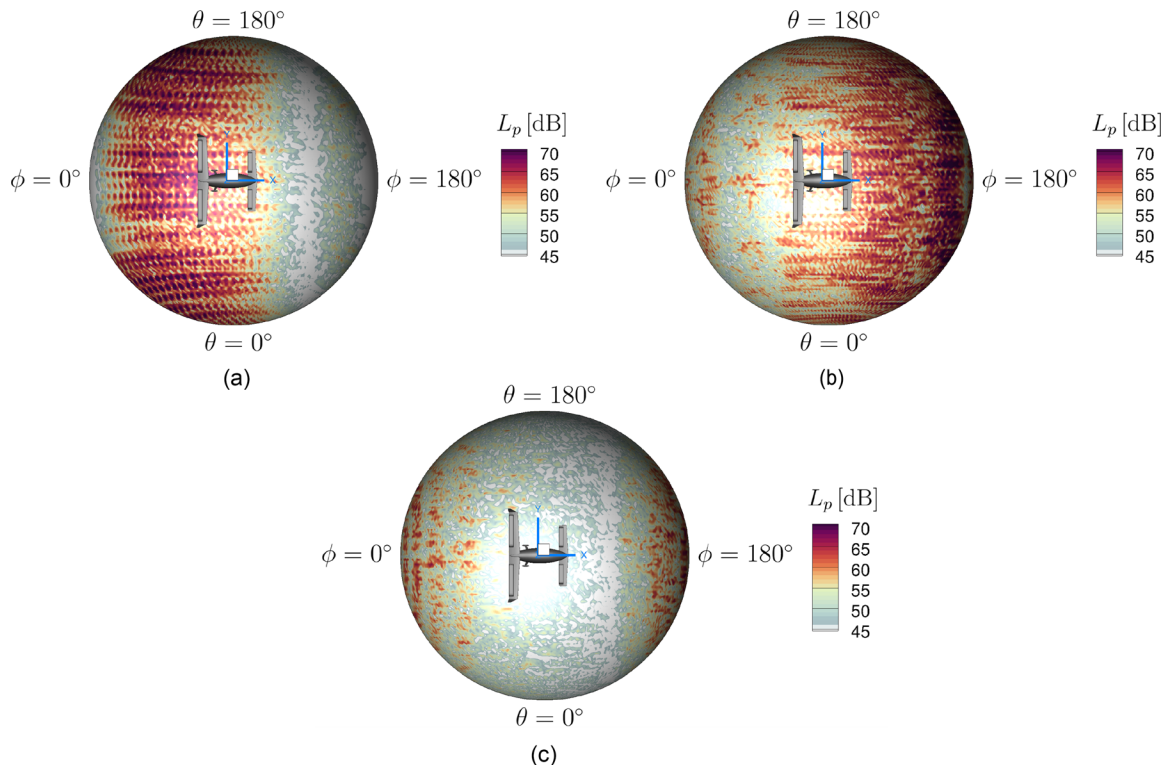


FIG. 14. Tonal noise directivities (sum over all frequencies) in the xy -plane at design conditions for the distributed propulsion system equipped with the baseline fan (a), low-broadband fan (b), and low-tone fan (c). Color scheme according to [Weninger \(2015\)](#).

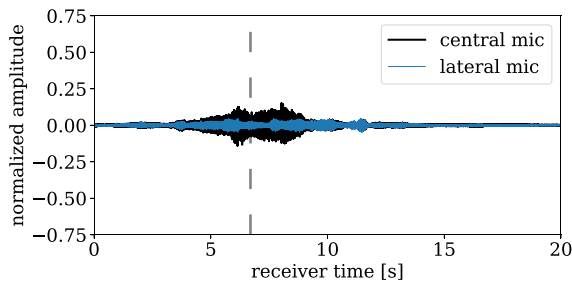


FIG. 15. Broadband time signal for the distributed propulsion system equipped with the baseline fan at the takeoff. The dashed vertical line denotes the time overhead. A value of 1.0 is equivalent to 94 dB.

$\pm 1\%$ is applied. The choice of the interval is based on the findings from Schade *et al.* (2024b).

If the distributed propulsion system is equipped with the baseline fan, the dominant tonal noise radiation direction is downstream and the peak radiation angle is $\phi = 50^\circ$. By contrast, if the low-broadband fan is used, the dominant tonal noise radiation direction changes to upstream with two peak radiation angles at $\phi = 135^\circ$ and $\phi = 165^\circ$. If the low-tone fan is used, the tonal noise radiation of the distributed propulsion system is significantly reduced over a wide range of radiation angles. However, tonal noise is still radiated upstream and downstream with peak radiation angles at $\phi = 30^\circ$ and $\phi = 170^\circ$. The dominant noise radiation angles of the distributed propulsion system correspond well with the peak radiation angles of the individual fan stages, which are analyzed by Schade *et al.* (2025).

Overall, irrespective of the fan design, the tonal noise directivities of the distributed propulsion systems show a stronger dependence on the axial than the lateral direction. For instance, when using the baseline fan, a lateral stripe

with almost constant tonal noise levels becomes visible at $\phi = 130^\circ$, and tonal noise increases abruptly for axial angles $\phi < 100^\circ$ independently of the lateral angle [see Fig. 14(a)]. This can be explained as only a few azimuthal modes are cut-on for tonal noise which are radiated into the far field.

As an intermediate conclusion, the noise emissions of the distributed propulsion systems are characterized by different tonal to broadband noise ratios and opposite dominant tonal noise radiation directions depending on the choice of the fan design. Thus, a strong dependence of the noise directivities on the axial and lateral emission angles is observed which is additionally intensified by complex acoustic interference patterns.

2. Noise immission

This section describes the noise exposure of the distributed propulsion systems at different microphone positions after propagating from the noise sources through the atmosphere (=noise immission) starting with the examination of broadband and tonal times signals. Spectral patterns are reported via spectrograms in a second step.

Figure 15 shows the broadband time signals at the central and lateral microphones for the distributed propulsion system equipped with the baseline fan. As the characteristic shapes of the broadband time signals of the three propulsion systems are very similar, they are exemplary shown for the baseline design. The only difference between the fan designs is a uniform reduction in sound pressure amplitudes for the low-broadband fan as already visualized in Fig. 13.

Overall, the broadband noise directivity is reflected in the time signal as again two maxima are observed, one before the microphone is passed at $t = 6$ s and one after the microphone is passed at $t = 8$ s. These maxima

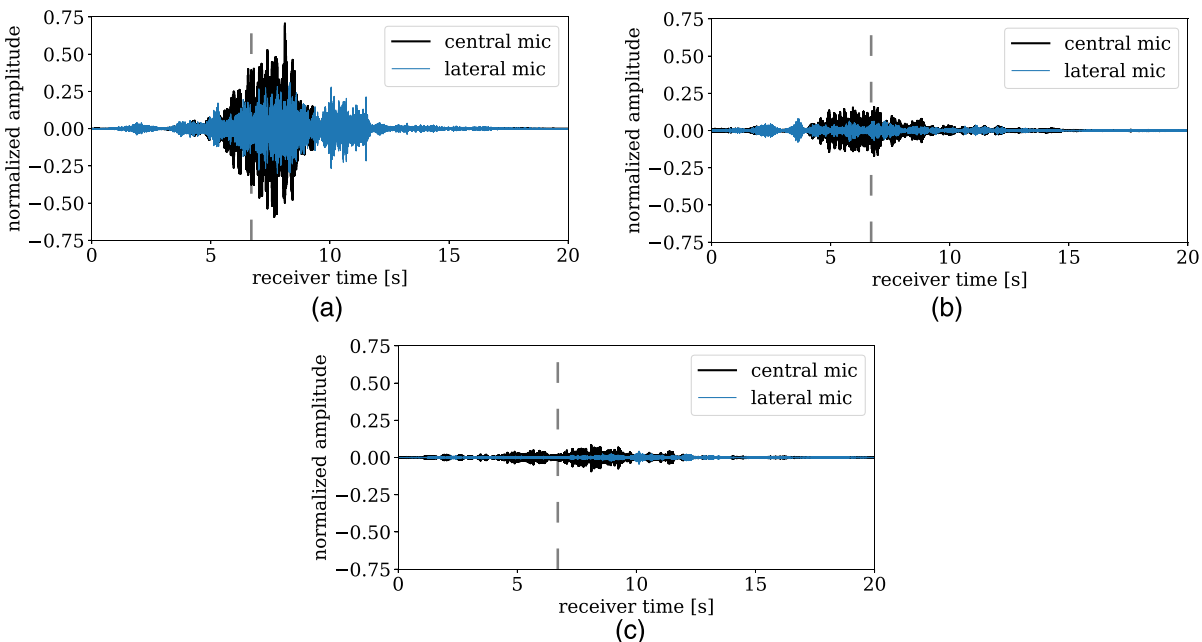


FIG. 16. Tonal time signal for the distributed propulsion system equipped with the baseline fan (a), low-broadband fan (b), and low-tone fan (c) at the take-off. The dashed vertical line denotes the time overhead. A value of 1.0 is equivalent to 94 dB.

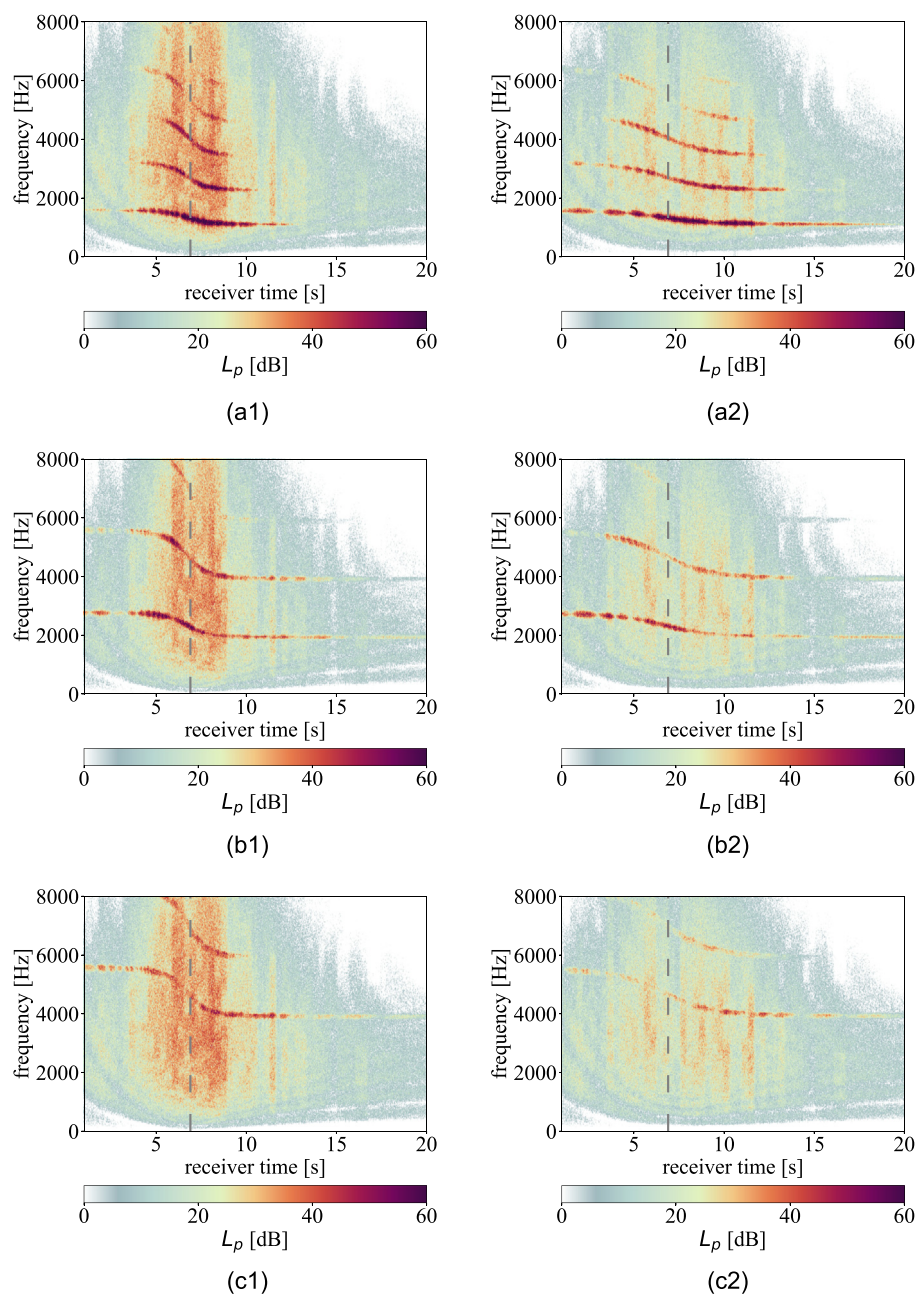


FIG. 17. (Color online) Spectrograms at the central (1) and lateral (2) microphones for the distributed propulsion system equipped with the baseline fan (a), low-broadband fan (b), and low-tone fan (c) at the takeoff. Color scheme according to Weninger (2015).

correspond to the radiation angles $\phi = 135^\circ$ and $\phi = 45^\circ$ [see Fig. 13(a)]. The broadband noise reaches a minimum at $t=6.5$ s which is the time when the microphone is reached indicated by the dashed line. This is equivalent with $\phi = 90^\circ$ in Fig. 13(a).

The tonal time signals for the three propulsion systems are plotted at the central and lateral microphone in Fig. 16, where the dashed line indicates the time when the microphone is reached. Again, the tonal noise directivities are reflected in the time signals. If the distributed propulsion system is equipped with the baseline fan, the highest tonal sound pressure amplitudes occur after the microphone is passed. Meanwhile, for the low-broadband fan, an opposite tonal time characteristic is observed. For the low-tone

design, the tonal sound pressure amplitudes are considerably lower than the broadband amplitudes over all times.

In order to assess not only temporal structures but also spectral patterns, Fig. 17 compares the monaural spectrograms between the different propulsion systems at the central and lateral microphones. The monaural spectrograms are provided to simplify the visualization, although the audio files are binaural (see Mm. 2, Mm. 3, and Mm. 4). The dashed vertical lines indicate the time overhead.

The spectrograms reflect the examined noise radiation characteristics of the three distributed propulsion systems. If the reference fan is used, the BPF tone and its harmonics are clearly visible and broadband noise is masked by the fan tones during all times of the flyover. If the low-broadband

TABLE III. Maximum tone-corrected perceived noise levels (PNLT_{max}) and effective perceived noise levels (EPNL) relative to the distributed propulsion system equipped with the baseline fan.

Fan design	ΔPNLT _{max} [dB]		ΔEPNL [dB]	
	Central	Lateral	Central	Lateral
Low-broadband	-8.2	-6.5	-7.0	-8.5
Low-tone	-13.0	-12.2	-11.7	-13.0

fan is used, the BPF tones are shifted to higher frequencies due to the increase in rotor blade count from 18 to 31. For the low-tone fan, the fan tones are shifted to even higher frequencies since the BPF tone is inverse cut-off, so that only the second and third harmonic are visible in the spectrogram. Overall, the tonal noise content is remarkably reduced resulting in a rather broadband-dominated noise immission, although, especially at the central microphone, the second blade passing frequency tone remains visible in the spectrogram [see 4000–5500 Hz in Fig. 17(c1)].

Comparing the central and lateral microphone positions, the main differences are the lower absolute noise levels at the lateral position, which are on the one hand due to the longer propagation distances leading to increased atmospheric absorption and spreading losses, and on the other hand due to the impact of the noise directivities, which show a stronger dependence on the axial direction than the lateral one (as visualized in Fig. 14).

For the acoustic certification of future aircraft with vertical takeoff and landing capabilities, as the considered UAM vehicle presented in Fig. 1, a new standard is currently under development (EASA, 2023). As suggested by EASA (2023), the noise evaluation metric is the effective

perceived noise level (EPNL) which is based on the tone-corrected perceived noise level (PNLT(t)). The maximum PNL_T values and EPNL are shown in Table III for the low-broadband and low-tone fan. The differences relative to the values of the baseline fan are given. For both fan designs, PNL_T_{max} and EPNL are remarkably reduced at the central and the lateral microphone positions. The EPNL is more than 7 dB lower if the distributed propulsion system is equipped with the low-broadband fan, and for the low-tone fan, an EPNL reduction of more than 11.7 dB is achieved.

3. Sound quality analysis

The values of the SQMs (as 5% percentiles) introduced in Sec. II C 4 are depicted in Fig. 18 for the three fan designs and both the central and lateral microphones. The presented values correspond to the takeoff procedure (see Table II, Fig. 7, and Sec. II C 2). In addition, a similar analysis is also performed for a horizontal flyover trajectory based on the EASA specifications (EASA, 2023). For the horizontal flyover the same specifications and limitations apply as for the takeoff procedure as listed in Sec. II C 2, however, Cruise operating conditions are considered as listed in Table II. Since similar trends are observed for the horizontal flyover as for the takeoff procedure, these results are not shown here for the sake of brevity.

For comparison purposes, the results for the SQM of sharpness, tonality, roughness, and fluctuation strength [Figs. 18(b)–18(e)] also include the experimental values of the Airbus A320 turbofan aircraft measured during takeoff from Fig. 11. The metrics of loudness and PA were not included in this comparison since they were considerably higher for the turbofan aircraft. For comparison with the turbofan case, it should be noted that different trajectories are

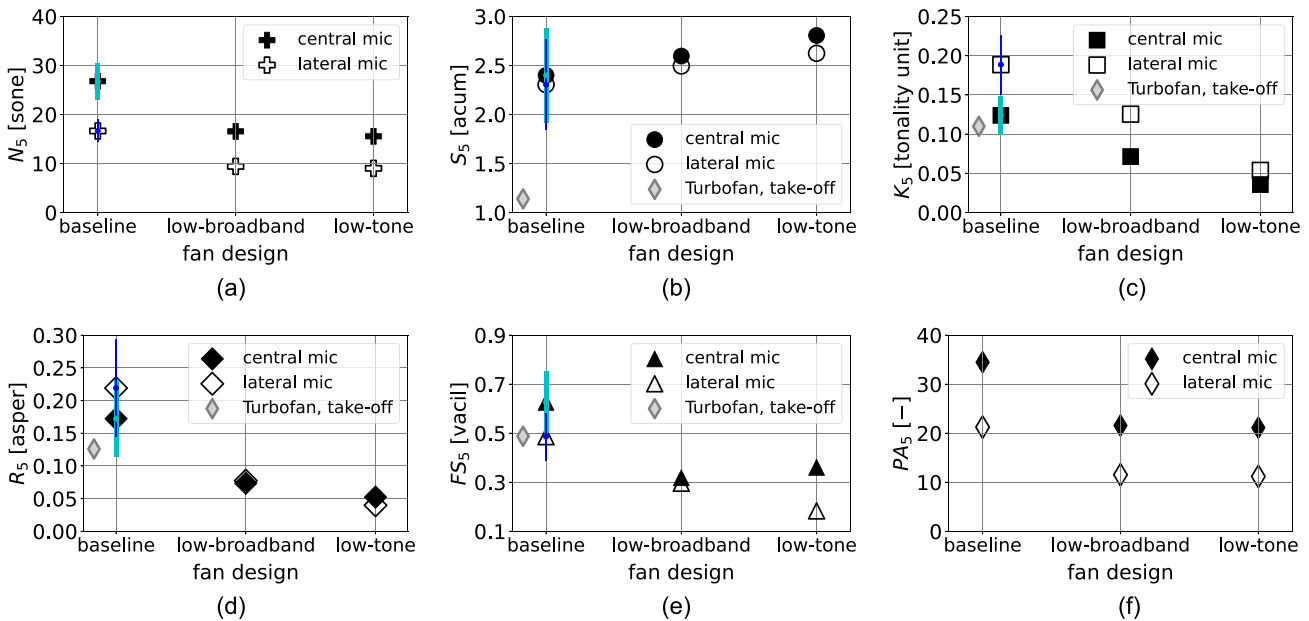


FIG. 18. Sound quality metrics [(a) loudness; (b) sharpness; (c) tonality; (d) roughness; (e) fluctuation strength] and psychoacoustic annoyance values (f) for each fan design and for the takeoff procedure. The values for the central and the lateral microphones are included. For the turbofan, the results from the measurements are re-plotted (see Fig. 11). For the baseline fan, the error bars refer to the JNDs, where each error bar is plotted as ± JND.

used, despite both being realistic takeoff trajectories (see Figs. 7 and 8).

In terms of loudness [Fig. 18(a)] both the low-broadband and low-tone fan designs achieve a reduction of roughly 40% in both microphone locations. Since loudness is the dominant SQM influencing the perceived noise annoyance (Greco *et al.*, 2023b), such a considerable reduction is expected to be perceived positively in practice. In comparison with the Airbus A320 takeoff validation case (Fig. 11), the UAM vehicle shows loudness values between two and three times lower for the central microphone, and even lower for the lateral microphone.

On the other hand, the sharpness values [Fig. 18(b)] experience an increase from roughly 2.4 acum for the baseline case to 2.6 and 2.8 acum for the low-broadband and low-tone cases, respectively. This is explained by the higher values of the BPF for the latter cases compared to the baseline, see Fig. 17. This is particularly relevant for the low-tone fan since the first BPF is (inverse) cut-off and only higher-frequency harmonics are present, hence, the acoustic energy is more distributed towards higher frequencies. In comparison, the turbofan aircraft presents a considerably lower sharpness value of 1.15 acum.

Regarding tonality [Fig. 18(c)], both the low-broadband and low-tone fan designs provide a considerable reduction with respect to the baseline. This is especially the case for the low-tone fan design, as expected, which offers a reduction in tonality of more than 70%, whereas the low-broadband fan design presents a lesser reduction of approximately 40%. It should be noticed that the tonality values at the lateral microphone (denoted as white markers) are consistently higher than those at the central microphone. This is explained by the relatively higher prominence of the tones for the lateral microphone shown in the spectrograms of Fig. 17, due to the noise radiation directivity patterns observed in Figs. 13 and 14. In contrast, the measured A320 takeoff procedure presents a tonality value (around 0.11 t.u.) similar to the baseline fan design case. It is interesting to note that the distributed propulsion system equipped with the baseline fan and the turbofan generate similar tonality values at takeoff conditions. On the one hand, for the baseline fan, the relatively high tonality value results from the blade passing frequency tone and its second, third and fourth harmonic which are the dominant tonal frequencies and which are well visible in the spectrogram (see Fig. 17). On the other hand, for the turbofan, the BPF tones and its harmonics are either cut-off or damped by a liner and are therefore not visible in the spectrogram [see Fig. 9(a)]. Thus, the buzz-saw tones, which are the dominant tonal frequencies for the turbofan, are responsible for the relatively high tonality value.

The two proposed fan designs also reduce the roughness metric compared to the baseline case [Fig. 18(d)]. Once again, the low-tone fan design has higher reductions (between 70% and 80% compared to the baseline) than the low-broadband one (between 55% and 65% compared to the baseline) for both microphone positions. With a roughness value of about 0.13 asper, the turbofan aircraft shows again

comparable values to the baseline fan design case. A similar behavior is observed for fluctuation strength [Fig. 18(e)] but with relatively smaller reductions: between 40% and 50% for the low-broadband design and between 42% and 62% for the low-tone one. The Airbus A320 takeoff presents again comparable values to the baseline fan design in terms of fluctuation strength, with a value of approximately 0.5 vacil. It should be noted that, since both metrics are based on amplitude modulations, the values of roughness and fluctuation strength are relatively sensitive to the rotational speed fluctuations within the fans, as discussed in Schade *et al.* (2024b).

Last, to classify the order of magnitude of a relevant change for each SQM, the JNDs are plotted in Fig. 18 as error bars showing the \pm JNDs. The JNDs indicate that the two low-count OGV fan stages (low-broadband and low-tone) offer reductions for all considered metrics well above one noticeable difference, despite a slight increase in sharpness which is, however, deemed as non-relevant since it is below one noticeable difference. The global psychoacoustic annoyance (PA) metric is evaluated for the three fan designs and the two microphone locations in Fig. 18(f). In this case, the decreases in PA obtained by the low-broadband and the low-tone fan designs with respect to the baseline case are virtually the same, with reductions of approximately 38% and 47% for the central and the lateral microphone, respectively. Despite the differences in sharpness, tonality, roughness, and fluctuation strength, the psychoacoustic annoyance model employed is strongly based on loudness (Di *et al.*, 2016; Merino-Martinez *et al.*, 2022), and since this metric is comparable in both fan designs [see Fig. 18(a)], the global PA values end up being very similar.

Comparing the reduction in PA from Fig. 18(f) with the reduction in PNL_{Tm} and EPNL from Table III, it is noticeable that the low-tone fan design leads to a considerable reduction in PNL_{Tmax} and EPNL compared to the low-broadband design at both microphones, whereas this is not reflected in the PA values, since both fans have almost identical PA values, as described above. Consequently, although a reduction of EPNL is observed, no reduction of PA between low-tone design and low-broadband design is determined. This confirms the initial hypothesis that propulsion designs with lower EPNL do not necessarily result in lower annoyance. However, the validity of the PA model formulated by Di *et al.* (2016) should be further examined in future listening tests.

Mm. 2. Binaural audio file of the distributed propulsion system equipped with the baseline fan at the central microphone of the takeoff procedure.

Mm. 3. Binaural audio file of the distributed propulsion system equipped with the low-broadband fan at the central microphone of the takeoff procedure.

Mm. 4. Binaural audio file of the distributed propulsion system equipped with the low-tone fan at the central microphone of the takeoff procedure.

V. SUMMARY AND CONCLUSION

In this paper, the acoustic characteristics of a distributed propulsion system of an urban air mobility vehicle were investigated. The considered propulsion system consists of 26 low-speed, ducted fan stages, where three acoustically different fan designs are examined: a baseline design, a low-broadband noise design, and a low-tonal noise design. The noise emissions of the distributed fan stages were predicted analytically, propagated through the atmosphere to a central and a lateral microphone using virtual flyover simulations and were auralized to obtain the audio recordings. To examine the perception of human hearing, several sound quality metrics were calculated. A validation of the auralization framework was provided based on measurement data from an A320 takeoff.

It was found that the distributed propulsion systems generate noise directivities with complex interference patterns showing a strong dependence on the axial and lateral angles. Compared to the distributed propulsion system equipped with the baseline fan, the low-broadband noise design achieves reductions of more than 6 dB for the maximum tone-corrected and effective perceived noise levels (PNLT_{max} and EPNL) at both microphones, whereas the low-tonal noise design achieves an even higher reduction of more than 11 dB. In addition, compared to the baseline design, the low-broadband and low-tonal noise designs reach a notable decrease in loudness, tonality, roughness, fluctuation strength, and, globally, psychoacoustic annoyance which is predicted by a model from Di *et al.* (2016). However, the reduction in PNL_{Tmax} and EPNL for the low-tonal noise design compared to the low-broadband noise design is not reflected in the psychoacoustic annoyance metric as both designs achieve similar values for psychoacoustic annoyance. Moreover, both fan designs showed higher levels of sharpness compared to the baseline design due to their relatively stronger high-frequency noise content.

Regarding the comparison with the A320 turbofan engines, comparable or even lower values of tonality, roughness and fluctuation strength are achieved for the low-broadband noise and low-tonal noise fan designs, whereas sharpness is notably increased for all distributed propulsion systems.

VI. OUTLOOK

The installation of the fans on the wings should be addressed in future studies and the impact of boundary layer ingestion (BLI) on the psychoacoustic characteristics of the propulsion system should be examined. The impact of BLI will affect all fan designs particularly the low-tone fan, as the tonal noise emission of this fan benefits from the inverse cut-off of the blade passing frequency tone. This acoustic effect could be neutralized by BLI as additional acoustic modes and noise sources will be excited (Quaroni *et al.*, 2024). This may result in stronger tonal noise radiation, which in turn may change the psychoacoustic characteristics of the propulsion system.

The fan noise emission, examined in Sec. IV B 1, is calculated using an analytical noise prediction method. These

results will be validated in future measurements conducted at CRAFT test facility. The measurements are already scheduled within the project VIRLWINT. As part of the measurement campaign, an inflow distortion representative for the boundary layer on the wing is designed to assess the impact of BLI on tonal noise emission for all considered fan designs. In addition to validating the noise emission, the measurement data also allows one to perform the auralization process chain not only with analytical input as in this paper, but also based on measured noise directivities so that the results can be compared and validated. Furthermore, airframe noise, neglected for this study, will be included in future auralizations as part of the ongoing DLR project LUFT 2030.

Regarding the distributed low-tone fans, the tonal noise levels are lower than the broadband levels for almost all radiation angles (see Sec. IV B 1), leading to lower sound pressure amplitudes at both microphones compared to the broadband amplitudes (see Sec. IV B 2) and to the lowest tonality and loudness values (see Sec. IV B 3). This offers the potential to design a liner not for a specific tonal frequency but for a wider frequency range to increase the acoustic attenuation of broadband noise, as for example examined by Sutliff *et al.* (2021).

To confirm the results obtained from the sound quality analysis and obtain new insights on the perceptual differences of the fan designs, psychoacoustic listening experiments with human subjects are of high interest and are planned for the near future. The low-broadband and low-tone fan designs are particularly suited for listening experiments as the loudness and psychoacoustic annoyance values are comparable between both designs, whereas other SQMs like roughness tonality or fluctuations strength are different. Therefore, such a psychoacoustic study would provide insights on the relative role of other SQMs while having similar loudness levels, as suggested by Boucher *et al.* (2024b).

ACKNOWLEDGMENTS

This publication is part of the project VIRLWINT (Virtual acoustical twin of distributed propulsion systems) funded by the German Aerospace Center (DLR). This publication is part of the project *Listen to the future* (project No. 20247) of the research program Veni 2022 (Domain Applied and Engineering Sciences) granted to R.M.-M. which is (partly) financed by the Dutch Research Council (NWO). In addition, the authors thank Patrick Ratei for providing the tilt-duct vehicle design from project VIRLWINT and we kindly acknowledge the help of Irina Besnea from Delft University of Technology for providing the experimental Airbus A320 flyover recording.

AUTHOR DECLARATIONS

Conflict of Interest

The authors state that they have no conflicts to disclose.

DATA AVAILABILITY

The data that support the findings of this study are available from the corresponding author upon request.

Arbeitsgruppe Novellierung der AzB (2007). *Anleitung Zur Berechnung Von Lärmschutzbereichen (AzB) [Instructions for Calculation of Noise Protection Areas (AzB)]* (Umweltbundesamt, Dessau-Roßlau, Saxony-Anhalt).

Aures, W. (1985). "Berechnungsverfahren für den sensorischen Wohlklang beliebiger Schallsignale" ("Calculation method for the sensory euphony of arbitrary sound signals"), *Acta Acust. united Acust.* **59**(2), 130–141.

Bernardini, G., Centracchio, F., Gennaretti, M., Iemma, U., Pasquali, C., Poggi, C., Rossetti, M., and Serafini, J. (2020). "Numerical characterisation of the aeroacoustic signature of propeller arrays for distributed electric propulsion," *Appl. Sci.* **10**(8), 2643.

Bernschütz, B. (2013). "A spherical far field HRIR/HRTF compilation of the Neumann KU 100," in *Proceedings of the 39th DAGA*, pp. 592–595.

Boucher, M. A., Christian, A. W., Krishnamurthy, S., Tracy, T., Begault, D. R., Shepherd, K., and Rizzi, S. A. (2024b). "Toward a psychoacoustic annoyance model for urban air mobility vehicle noise," technical report No. NASA TM–20240003202, ntrs.nasa.gov/api/citations/20240003202/downloads/NASA-TM-20240003202June.pdf (Last viewed October 2, 2024).

Boucher, M., Rafaelof, M., Begault, D., Christian, A., Krishnamurthy, S., and Rizzi, S. (2024a). "A psychoacoustic test for urban air mobility vehicle sound quality," *SAE Int. J. Adv. Curr. Prac. Mobility* **6**(2), 972–985.

Caldas, L., Kruck, S., Klähn, L., Rudolphi, A., Meyer, R., Enghardt, L., and Tapken, U. (2022). "Construction and assessment of an inflow-control-device for a low-speed aeroacoustic fan rig," *AIAA J.* **60**(9), 5299–5312.

Dang, M. (2022). "Usability and maintainability of the software tools violin and coral," Bachelor thesis, Baden-Württemberg Cooperative State University, Stuttgart, Baden-Württemberg, Germany.

Daniel, P., and Webber, R. (1997). "Psychoacoustical roughness: Implementation of an optimized model," *Acust. Acta Acust.* **83**, 113–123.

Di, G.-Q., Chen, X.-W., Song, K., Zhou, B., and Pei, C.-M. (2016). "Improvement of Zwicker's psychoacoustic annoyance model aiming at tonal noises," *Appl. Acoust.* **105**, 164–170.

EASA (2023). "Environmental protection technical specifications applicable to VTOL-capable aircraft powered by tilting rotors," consultation paper No. 1.

Eißfeldt, H., and Stolz, M. (2024). "Public perception of air taxis in Germany: Anticipated risks, benefits, and noise sensitivity," *Proc. Mtg. Acoust.* **54**(1), 040004.

Fastl, H., and Zwicker, E. (2007). *Psychoacoustics—Facts and Models*, 3rd ed. (Springer-Verlag, Berlin).

Giacche, D., Hynes, T. P., Baralon, S., Coupland, J., Humphreys, N., and Schwaller, P. (2013). "Acoustic optimization of ultra-low count bypass outlet guide vanes," in *19th AIAA/CEAS Aeroacoustics Conference*.

Greco, G. F., Merino-Martinez, R., and Osses, A. (2023a). "SQAT: A sound quality analysis toolbox for MATLAB," available at github.com/greco/sqat (Last viewed May 3, 2023).

Greco, G. F., Merino-Martinez, R., and Osses, A. (2024). "SQAT: A sound quality analysis toolbox for MATLAB (version v1.1)," available at [http://dx.doi.org/10.5281/zenodo.10580337](https://dx.doi.org/10.5281/zenodo.10580337) (Last viewed May 20, 2024).

Greco, G. F., Merino-Martinez, R., Osses, A., and Langer, S. C. (2023b). "SQAT: A MATLAB-based toolbox for quantitative sound quality analysis," in *52nd International Congress and Exposition on Noise Control Engineering* (August 20–23) [International Institute of Noise Control Engineering (I-INCE), Chiba, Greater Tokyo, Japan].

Guérin, S., and Tormen, D. (2023). "A contribution to the investigation of acoustic interferences in aircraft distributed propulsion," *CEAS Aeronaut. J.* **14**, 965–982.

Gwak, D. Y., Han, D., and Lee, S. (2020). "Sound quality factors influencing annoyance from hovering UAV," *J. Sound Vib.* **489**, 115651.

Heidmann, M. F. (1975). "Interim prediction method for fan and compressor source noise," NASA technical memorandum X-71763, available at ntrs.nasa.gov/citations/19750017876 (Last viewed October 2, 2024).

Hornikx, M. (2016). "Ten questions concerning computational urban acoustics," *Build. Environ.* **106**, 409–421.

ICAO (2017). "Annex 16 to the convention on international civil aviation, environmental protection," in *Aircraft Noise*, 8th ed. (International Civil Aviation Organization, Montréal, Canada), Vol. 1.

ISO 532-1 (2017). "Acoustics—Method for calculating loudness—Zwicker method" (International Organization for Standardization, Geneva, Switzerland).

ISO 9613-1 (1993). "Attenuation of sound during propagation outdoors, Part 1: Calculation of the absorption of sound by the atmosphere" (International Organization for Standardization, Geneva, Switzerland).

Jaron, R. (2018). "Aeroakustische Auslegung von triebwerksfans mittels multidisziplinärer optimierungen" ("Aeroacoustic design of engine fans by means of multidisciplinary optimizations"), *Dissertation*, Technical University of Berlin, Berlin, Germany.

Merino-Martinez, R., Ben-Gida, H., and Snellen, M. (2024a). "Psychoacoustic evaluation of an optimized low-noise drone propeller design," in *30th International Congress on Sound and Vibration (ICSV)*, Amsterdam, The Netherlands (July 8–11).

Merino-Martinez, R., Besnea, I., von den Hoff, B., and Snellen, M. (2024b). "Psychoacoustic analysis of the noise emissions from the Airbus A320 aircraft family and its nose landing gear system," in *30th AIAA/CEAS Aeroacoustics Conference*, AIAA paper 2024–3398, Rome, Italy (June 4–7).

Merino-Martinez, R., Pieren, R., and Schäffer, B. (2021). "Holistic approach to wind turbine noise: From blade trailing-edge modifications to annoyance estimation," *Renew. Sustain. Energy Rev.* **148**(111285), 111285.

Merino-Martinez, R., Pieren, R., Schäffer, B., and Simons, D. G. (2022). "Psychoacoustic model for predicting wind turbine noise annoyance," in *The 24th International Congress on Acoustics (ICA)*, Gyeongju, South Korea (October 24–28), www.researchgate.net/publication/364996997_Psychoacoustic_model_for_predicting_wind_turbine_noise_annoyance (Last viewed October 21, 2024).

Merino-Martinez, R., Yupa-Villanueva, R. M., von den Hoff, B., and Pockelé, J. S. (2024c). "Human response to the flyover noise of different drones recorded in field measurements," in *3rd Quiet Drones Conference*, Manchester, UK (September 8–11).

Monteiro, F. d N., Merino-Martinez, R., and Lima Pereira, L. T. (2024). "Psychoacoustic evaluation of an array of distributed propellers under synchrophasing operation," in *30th AIAA/CEAS Aeroacoustics Conference*, AIAA paper 2024–3321, Rome, Italy (June 4–7).

Moreau, A. (2017). "A unified analytical approach for the acoustic conceptual design of fans for modern aero-engines," *Dissertation*, Technical University of Berlin, Berlin, Germany.

Moreau, A., Prescher, A., Schade, S., Dang, M., Jaron, R., and Guérin, S. (2023a). "A framework to simulate and to auralize the sound emitted by aircraft engines," in *InterNoise Conference 2023*.

Moreau, A., Schnell, R., and Mennicken, M. (2023b). "Acoustic preliminary design of a low-noise fan stage considering a variable-area nozzle and variable-pitch rotor blades," *CEAS Aeronaut. J.* **14**, 325–341.

Nallasamy, M., Envia, E., Thorp, S., and Shabbir, A. (2002). "Fan noise source diagnostic test—Computation of rotor wake turbulence noise," in *8th AIAA/CEAS Aeroacoustics Conference & Exhibit*.

OpenSky (2025). <https://opensky-network.org/> (Last viewed September 2021).

Osses, A., Greco, G. F., and Merino-Martinez, R. (2023). "Considerations for the perceptual evaluation of steady-state and time-varying sounds using psychoacoustic metrics," in *10th Convention of the European Acoustics Association (Forum Acusticum)*, Torino, Italy (September 11–15).

Osses Vecchi, A., García León, R., and Kohlrausch, A. (2017). "Modelling the sensation of fluctuation strength," *Proc. Mtgs. Acoust.* **28**(1), 050005.

Pascioni, K., and Rizzi, S. A. (2018). "Tonal noise prediction of a distributed propulsion unmanned aerial vehicle," in *2018 AIAA/CEAS Aeroacoustics Conference*.

Prescher, A., Moreau, A., and Schade, S. (2024). "Model extension of random atmospheric inhomogeneities during sound propagation for engine noise auralization," *CEAS Aeronaut. J.* **15**, 1111–1125.

Quaroni, L. N., Merino-Martinez, R., Monteiro, F. d N., and Kumar, S. S. (2024). "Collective blade pitch angle effect on grid turbulence ingestion noise by an isolated propeller," in *30th AIAA/CEAS Aeroacoustics Conference*, AIAA paper 2024–3209, Rome, Italy (June 4–7).

- Ratei, P. (2022). "Development of a vertical take-off and landing aircraft design tool for the application in a system of systems simulation framework," Master thesis, Hamburg University of Applied Sciences, Haw, Hamburg, available at elib.dlr.de/186947/ (Last viewed September 18, 2024).
- Ratei, P., Naeem, N., and Prakasha, P. S. (2023). "Development of an urban air mobility vehicle family concept by system of systems aircraft design and assessment," *J. Phys. Conf. Ser.* **2526**(1), 012043.
- Rietdijk, F., Forssén, J., and Heutschi, K. (2017). "Generating sequences of acoustic scintillations," *Acta Acust. united Acust.* **103**(2), 331–338.
- Rizzi, S. A. (2016). "Toward reduced aircraft community noise impact via a perception-influenced design approach," in *Inter-Noise 2016*, available at ntrs.nasa.gov/citations/20160011152 (Last viewed September 18, 2024).
- Rizzi, S. A., Huff, D. L., Boyd, D. D., Bent, P., Henderson, B. S., Pascioni, K. A., Sargent, D. C., Josephson, D. L., Marsan, M., He, H., and Snider, R. (2020). "Urban air mobility noise: Current practice, gaps, and recommendations," NASA/TP-2020-5007433.
- Schade, S., Jaron, R., Klähn, L., and Moreau, A. (2024a). "Smart blade count selection to align modal propagation angle with stator stagger angle for low-noise ducted fan designs," *Aerospace* **11**(4), 259.
- Schade, S., Jaron, R., Moreau, A., and Guérin, S. (2022). "Mechanisms to reduce the blade passing frequency tone for subsonic low-count OGV fans," *Aerosp. Sci. Technol.* **125**, 107083.
- Schade, S., Ludowicy, J., Ratei, P., Hepperle, M., Stürmer, A., Rossignol, K.-S., de Graaf, S., and Geyer, T. F. (2025). "Conceptual design of electrically-powered urban air mobility vehicles for aeroacoustic studies," CEAS Aeronaut. J. (in press).
- Schade, S., Merino-Martinez, R., Ratei, P., Bartels, S., Jaron, R., and Moreau, A. (2024b). "Initial study on the impact of speed fluctuations on the psychoacoustic characteristics of a distributed propulsion system with ducted fans," in *30th AIAA/CEAS Aeroacoustics Conference*.
- Shiva Prakasha, P., Naeem, N., Ratei, P., and Nagel, B. (2022). "Aircraft architecture and fleet assessment framework for urban air mobility using a system of systems approach," *Aerosp. Sci. Technol.* **125**, 107072.
- Soeta, Y., and Kagawa, H. (2020). "Three dimensional psychological evaluation of aircraft noise and prediction by physical parameters," *Build. Environ.* **167**, 106445.
- Sutliff, D. L., Nark, D. M., and Jones, M. G. (2021). "Multi-degree-of-freedom liner development: Concept to flight test," *Int. J. Aeroacoust.* **20**(5-7), 792–825.
- Tapken, U., Caldas, L., Meyer, R., Behn, M., Klähn, L., Jaron, R., and Rudolphi, A. (2021). "Fan test rig for detailed investigation of noise generation mechanisms due to inflow disturbances," in *AIAA Aviation 2021 Forum*.
- Torija, A. J., and Clark, C. (2021). "A psychoacoustic approach to building knowledge about human response to noise of unmanned aerial vehicles," *Int. J. Environ. Res. Public Health* **18**(2), 682.
- Torija, A. J., Roberts, S., Woodward, R., Flindell, I. H., McKenzie, A. R., and Self, R. H. (2019). "On the assessment of subjective response to tonal content of contemporary aircraft noise," *Appl. Acoust.* **146**, 190–203.
- Tyler, J. M., and Sofrin, T. G. (1962). "Axial flow compressor noise studies," *SAE Technical Paper* 620532.
- von Bismark, G. (1974). "Sharpness as an attribute of the timbre of steady sounds," *Acta Acust. united Acust.* **30**(3), 159–172.
- Vorländer, M. (2008). *Auralization—Fundamentals of Acoustics, Modelling, Simulation, Algorithms and Acoustic Virtual Reality*, 1st ed. (Springer, Berlin).
- Weninger, B. (2015). "A color scheme for the presentation of sound immersion in maps: Requirements and principles for design," in *EuroNoise 2015*, available at <https://www.conforg.fr/euronoise2015/proceedings/data/articles/000069.pdf> (Last viewed September 12, 2024), pp. 439–444.
- Yang, H., Nuernberger, D., and Kersken, H.-P. (2006). "Toward excellence in turbomachinery computational fluid dynamics: A hybrid structured-unstructured Reynolds-averaged Navier-Stokes solver," *J. Turbomach.* **128**(2), 390–402.